An Electrical Bioimpedance Scanning System for Subsurface Tissue Detection in Robot Assisted Minimally Invasive Surgery

Zhuoqi Cheng ⓘ, Kim Lindberg Schwaner ⓘ, Diego Dall'Alba ⓘ, Paolo Fiorini ⓘ, and Thiusius Rajeeth Savarimuthu ⓘ

Abstract—**In Robot Assisted Minimally Invasive Surgery, discriminating critical subsurface structures is essential to make the surgical procedure safer and more efficient. In this paper, a novel robot assisted electrical bio-impedance scanning (RAEIS) system is developed and validated using a series of experiments. The proposed system constructs a tri-polar sensing configuration for tissue homogeneity inspection. Specifically, two robotic forceps are used as electrodes for applying electric current and measuring reciprocal voltages relative to a ground electrode which is placed distal from the measuring site. Compared to existing electrical bioimpedance sensing technology, the proposed system is able to use miniaturized electrodes to measure a site flexibly with enhanced subsurfacial detection capability. This paper presents the concept, the modeling of the sensing method, the hardware design, and the system calibration. Subsequently, a series of experiments are conducted for system evaluation including finite element simulation, saline solution bath experiments and experiments based on ex vivo animal tissues. The experimental results demonstrate that the proposed system can measure the resistivity of the material with high accuracy, and detect a subsurface non-homogeneous object with 100% success rate. The proposed parameters estimation algorithm is able to approximate the resistivity and the depth of the subsurface object effectively with one fast scanning.**

Index Terms—**Electrical bioimpedance sensing, robotic assisted sensing, tri-polar measurement, subsurface tissue detection.**

I. INTRODUCTION

THANKS to the enhanced precision, flexibility and controllability, Robot Assisted Minimally Invasive Surgery

(RAMIS) has regularly been exploited for many types of complex surgical treatments. With the help of robotic technology, surgeons are able to perform delicate and complex procedures that may have been difficult or impossible with other methods. This is confirmed by the constant increase in RAMIS systems installed in hospitals worldwide and by their use in clinical areas other than those initially adopted (i.e. urology and gynecology) [1]. Also, patients undertaking RAMIS have reported less pain, smaller incision, shorter hospital stay, and lower postoperative morbidity [2]. Despite all the advantages described, there are also some limitations of the current clinical RAMIS, in particular related to intra-operative perception technologies [3]. In RAMIS, the robot replaces the surgeon in accessing the surgical environment. The surgeon has limited perception and tactile feedback, mainly based on endoscopic stereo images. Thus, it remains a big challenge for surgeons to find and detect critical subsurface tissues. For instance, stage II and stage III cancers can grow deeply into nearby tissue and also spread to lymph nodes [4]. Surgeries to remove these pathological tissues often take time, especially, to find and localize the pathological tissues [5]. In addition, hidden blood vessels are difficult to be detected and can accidentally be damaged during the execution of the surgical procedure. The consequence can be various surgical complications, and in the worst case scenario lead to patient death [6].

To overcome the above obstacles, intra-operative imaging facility such as Magnetic Resonance Imaging (MRI) [7] or Computer Tomography (CT) [8] is used to guide the surgery while the patient is undergoing a procedure. Thereby, the risk of damaging critical subsurfacial parts can be reduced significantly, and the surgeons are able to confirm the correct execution of most critical steps (e.g. complete tumor resection) before the surgery is completed. However, the imaging facility is not always available and is not compatible with most surgical robots. Additionally, the intra-operative identification of critical tissue has been explored using pre-operative information registered on the patient and visualized by means of Augmented Reality (AR) systems [9]. However, its application is constrained by the complicated image registration algorithms and heavy computation load. The medical requirements of accuracy are hard to satisfy due to tissue deformation [10]. In addition to the above methods, real-time and on-site tissue identification technologies

such as fluorescence technology, are significantly improving the surgical quality and efficiency [11]. By injecting an exogenous contrast agent to the targeted tissue region, the fluorophores within the region absorb UV and visible light and re-emit some of this light at longer wavelengths. The reflected illumination light can highlight the neoplasia, yielding to enhanced optical screening of surface tumors [12]. Unfortunately, the infrared light can only penetrate a few millimeters, and thus it may not be feasible for finding structures (e.g. vessels or highly perfusive regions) in a relatively deep region [13]. In addition to the above, various intra-operative sensing probes have been developed as an important component for improving current and future RAMIS systems [14]. For instance, a drop-in ultrasound transducer (X12C4) is developed by BK Medical Inc., which can be grasped by the robotic arm to scan and navigate during RAMIS [15]. The problem for such an ultrasound transducer is that it is generally expensive, and special training is required to manipulate the probe and understand the ultrasound images [16]. Also, various palpation probes have been developed for detecting harder region of the tissue such as [17], [18]. However, only a limited number of these devices have been tested in the clinical settings.

Another recently developed sensing technology for tissue identification is the Electrical Bioimpedance (EBI) sensing [19]. It senses the electrical characteristics of biological material by measuring the response to the flow of an applied alternating electrical current with a given amplitude and frequency. This sensing technology features compact size, low cost, fast response and high sensitivity. Previous studies have demonstrated its efficacy in many clinical applications such as venipuncture detection [20], cancer detection [21], stage monitoring in bone drilling [22] and glucose measurement [23].

In addition, researchers from the Dartmouth group [24] have developed an endoscopic probe which can be use for surgical margin assessment based on Electrical Impedance Tomography (EIT). Although the probe has been demonstrated to distinguish healthy and tumorous tissues effectively, the sensing capability in depth is limited due to size of the probe. Our previous studies [25], [26] have successfully integrated the EBI sensing into a surgical robot for real time intra-operative tissue identification. However, since a bi-polar EBI sensing method is used, the reliability of EBI sensing depends on a precise control of the contacting area between the sensing electrode and the tissue [27]. This is generally difficult due to tissue deformation.

In this paper, we present a Robot Assisted Electrical bio-Impedance Sensing (RAEIS) system as shown in Fig. 1. Compared to the previous study [25], the new EBI sensing system employs two standard surgical instruments with electrosurgical function (such as mono-polar or bi-polar forceps) as electrodes. One electrode is used for providing a current source and the other electrode is for measuring voltage on the tissue surface. Both current source and measured voltages are referred to a third sink electrode positioned in a distal region with respect to the measurement site. According to the authors' best knowledge, the proposed sensing method is the world's first design for tissue resistivity measurement and interpretation based on a tripolar configuration and existing RAMIS instruments. Unlike other
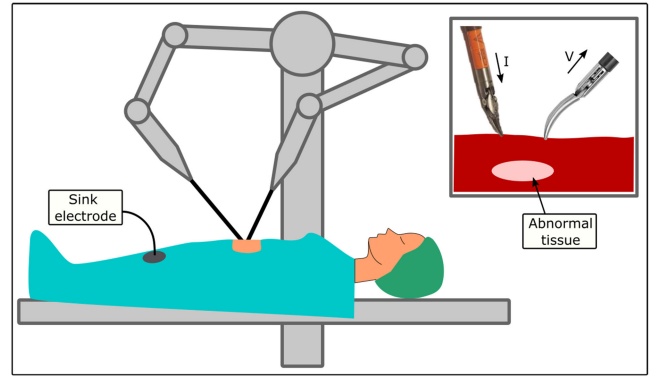

Fig. 1.   Detecting subsurface abnormal tissue is challenging during a RAMIS.

existing technologies [28], the proposed method utilizes flexible separate electrodes, and is based on coordinated control for measurement and data analysis. The advantages of the proposed RAEIS system include simple setup, easy integration, low cost, online sensing, and little modifications to the existing hardware. Since electrodes are controlled separately, they can be miniaturized to enter small orifices while detection accuracy can be maintained. Compared to the other EBI or EIT sensing systems, the proposed sensing system has an enhanced sensing capability and autonomy. Based on the enhanced flexibility and sensing capability, the proposed system can be used for measuring tissue electrical resistivity in a local region and for the detection of subsurface non-homogeneous structure.

The rest of the paper is organized as follows: Section II introduces the methodology, modelling and hardware. Also, different design parameters are interpreted and system calibration is provided. Subsequently, a series of experiments are designed and performed for the system evaluation in Section III. Section IV provides the experimental results. Section V discusses the results and Section VI concludes this paper.

II. METHODS

A. Tri-Polar EBI Sensing

Compared to a bi-polar EBI sensing configuration which couples two electrodes to inject differential excitation signal and measure the reciprocal signal, a tri-polar EBI sensing configuration contains three electrodes, two of which are used for current excitation and the other one is used for measuring the electric potential. Fig. 2(a) shows the schematic of the bipolar EBI sensing system. In the excitation frequency range of β dispersion (about 1 kHz to 1 MHz, see [29]), the measured EBI normally involves a polarization impedance (Z_{el}) serialising the Material Under Test (MUT) due to the interfacial layers between the metal electrode and the tissue, which are known as Helmholtz layer and Gouy-Chapman layer [30]. Therefore, the resistance of the MUT is hard to measure accurately using a bi-polar EBI configuration. In the proposed tri-polar sensing system (Fig. 2(b)), the excitation source and the voltage measurement are separated [31], [32]. By doing so, the effects of Z_{el} can be compensated for by using a controlled current source to maintain a constant current through
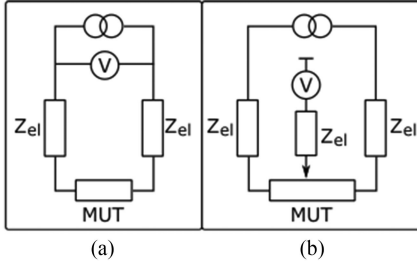
Fig. 2. (a) Schematics of a bi-polar EBI sensing. (b) Schematics of a tri-polar EBI sensing.
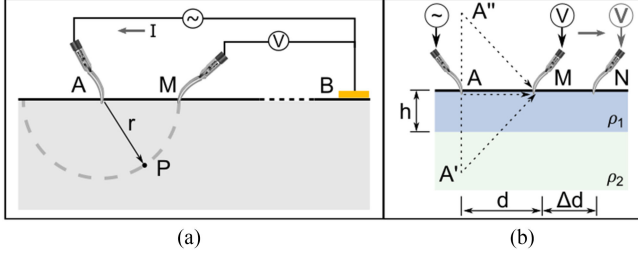

Fig. 3. (a) Modeling the EBI measurement using a half-Schlumberger electrode array. (b) The measurement on two materials ρ_1 and ρ_2.

the MUT. In addition, the input impedance for the electrical potential measurement can be made very high to avoid current flows through the voltage monitor electrode. Thus, the generated electric field is not affected by the contact between the electrodes and tissue.

The current source electrode and voltage measuring electrode can be realized by two separate surgical forceps/tools. This allows the system to measure the targeted site flexibly. Also, through adjusting the distance between the two electrodes, the measured impedance covers a different range of materials, and thus enables the sensing of subsurface tissue at different depths. More technical details are provided below.

B. Modelling

The sensing technology for detecting the subsurface tissue in this study is inspired by the electrical survey method used in geophysics, where the electrode configuration and method is commonly known as the Wenner-Schlumberger array [33]. As shown in Fig. 3(a), a current I passes through the tissue via the electrode pair A and B. Furthermore, when the sink electrode B is located far away from the measurement site ($|AB| > 5|AM|$), the sensing configuration is also known as half-Schlumberger electrode configuration. In this case, assuming that the tissue under measurement is homogeneous, the current flow disperses from the source A radially into the tissue. The current distribution is uniform over hemispherical shells centred on the source. Thus, at a distance r from A, the current density at point P is given by

$$J_p = \frac{I}{2\pi r^2} \tag{1}$$

According to the Maxwell's equations, the electrical potential of a point P in a medium of uniform resistivity ρ can be

calculated by integrating (1).

$$V_P = -\int_{r_0}^{r} \frac{\rho I \partial r}{2\pi r^2} = \frac{I\rho}{2\pi r} - \frac{I\rho}{2\pi r_0} \tag{2}$$

where r_0 represents the equivalent radius of the electrode. To get rid of the impact of r_0, the potential difference is used for the calculation here. Considering that the potentials of 2 positions on the surface M and N are measured, the electrical potential difference is

$$V_{MN} = \frac{I\rho}{2\pi} \left(\frac{1}{|AM|} - \frac{1}{|AN|} \right) = \frac{I\rho}{2\pi} \left(\frac{1}{d} - \frac{1}{d + \Delta d} \right) \tag{3}$$

Here, we use d and Δd to denote the distance of $|AM|$ and $|MN|$ respectively. The resistivity of the material measured by electrodes A, M and N can be calculated as

$$\rho_a(d) = \frac{2\pi V_{MN} d(d + \Delta d)}{I\Delta d} \tag{4}$$

The resistivity $\rho_a(d)$ calculated from (4) is also known as the apparent resistivity, which reflects the observed resistivity of the MUT measured at a distance d. This value ought to be constant given that the MUT is uniform.

For the case where there is a second layer of abnormal tissue at depth h, as shown in Fig. 3(b), the potential at point M due to the current introduced from A includes two parts: the direct current flow along the path AM and the part caused by the reflected current [33]. The reflecting part can be calculated as an intensity-reduced current introduced from an image point A' in the medium ρ_2 at depth $2h$. According to [34], the two parallel interfaces between ρ_1 and ρ_2 and between ρ_1 and the air can produce an infinite series of images of the source. Here, ρ_1 and ρ_2 represent the electrical resistivity of the superficial and subsurface tissues respectively. In the interface between ρ_1 and ρ_2, the intensity of the reflected current is reduced by a factor k, which is also known as the reflection coefficient of the interface:

$$k = \frac{\rho_2 - \rho_1}{\rho_1 + \rho_2} \tag{5}$$

In addition, the reflected current reaches the interface between ρ_1 and the air, and a total reflection occurs. Part of the reflected current would flow to M. This can be understood as another image point A'' which is located $2h$ above the tissue surface broadcasts the same intense current to the measurement point M as shown in Fig. 3(b). Therefore, the electrical potential at point M can be calculated as:

$$V_M = \frac{I\rho_1}{2\pi} \left(\frac{1}{d} + 2 \sum_{n=1}^{\infty} \frac{k^n}{\sqrt{d^2 + (2nh)^2}} \right) \tag{6}$$

The electric potential at another point N can be calculated in the same way, and thus the voltage difference between point M and N can be rewritten as:

$$V_{MN}^* = \frac{I\rho_1}{2\pi} \left[\frac{\Delta d}{d(d + \Delta d)} + 2 \sum_{n=1}^{\infty} \left(\frac{k^n}{\sqrt{d^2 + (2nh)^2}} \right. \right.$$
$$\left. \left. - \frac{k^n}{\sqrt{(d + \Delta d)^2 + (2nh)^2}} \right) \right] \tag{7}$$

Substituting (7) into (4) and simplifying the result, we have

$$\rho_a(d) = \rho_1 \left[1 + 2\frac{d(d+\Delta d)}{\Delta d} \sum_{n=1}^{\infty} \left(\frac{k^n}{\sqrt{d^2+(2nh)^2}} \right. \right.$$
$$\left. \left. - \frac{k^n}{\sqrt{(d+\Delta d)^2+(2nh)^2}} \right) \right] = \rho_1(1+\alpha) \quad (8)$$

where α is used to denote a part of (8) for making the equation concise. According to (8), the calculated apparent resistivity contributed by the reflected current is associated to the ratio of d and h. When d is small, especially $d \ll h$, ρ_a is approximately equal to ρ_1. It represents the electrical resistivity of the superficial material. By increasing the distance between two electrodes, the ratio of d/h becomes bigger, and thus the reflected current contributes a bigger portion to the calculated apparent resistivity. However, the setting of d should have an upper bound. This is because if d is set too big, the consequent V_{MN} can be too small to be measured accurately.

We can calculate the relative standard deviation of $\rho_a(d)$ along d as the criteria Γ for the detection of subsurface non-homogeneous material. We assume that the measurements are conducted on N different locations from d_1 to d_N, and $\rho_a(d_i)$ is the apparent resistivity obtained at d_i.

$$\Gamma = \frac{\sqrt{\frac{\sum_{i=1}^{N}(\rho_a(d_i)-\mu)^2}{N}}}{\mu} \quad (9)$$

where μ is the mean value of observations $\rho_a(d)$ with d from d_1 to d_N. As indicated in (9), Γ should be very small if the MUT is homogeneous. If there is a subsurface layer of different tissue, the change of ρ_a along d is summed up and results to a relatively big value of Γ.

C. Parameters Estimation

Potentially, the calculated values $\rho_a(d)$ can be used to estimate the resistivity and the depth of the second layer material. The strategy of the algorithm is to search a set of candidate models, $\tilde{\rho}_a(d)$, comprising different parameter combinations and calculate its fitting accuracy with respect to the real measurement $\rho_a(d)$. A subset of possibilities are constructed by equal sampling of ρ_1, k, h. The best performer with the highest predictive accuracy is used to estimate the parameters.

The scheme of the search algorithm is presented in Algorithm 1. Firstly, we determine whether the subsurface material has a higher or lower resistivity compared to the superficial material based on (8). Assuming that the scanning is performed from $d = d_0$ to d_1 ($d_0 < d_1$), the subsurface material is less conductive if $\rho_a(d_1)$ is bigger than $\rho_a(d_0)$, and vice versa. Secondly, we generate a pool of candidates by conducting an equal sampling of different parameters including the resistivity of the superficial layer ρ_1, the reflection coefficient k, and the depth of the second layer h. Based on (8), ρ_1 can be rewritten as $\rho_1 = \rho_a(d)/(1+\alpha)$ with $d = d_0$ to represent the measurement of the superficial layer. Specifically, the range of α should be between 0 and $2k/(1-k)$ according to the definition of reflection coefficient. The range of k should be either $0 < k < 1$ for the case when

---

Algorithm 1: Pool of Candidates Generation.

if $\rho_a(d_1) > \rho_a(d_0)$ **then**
  $k^* = 1$
else
  $k^* = -1$
end if
for $k = 0$ to k^* **do**
  for $\alpha = 0$ to $2k/(1-k)$ **do**
    $\rho_1 = \rho_a(d_0)/(1-\alpha)$
    for $h = 0$ to d_1 **do**
      for $d = d_0$ to d_1 **do**
        calculate $\tilde{\rho}_a(d)$ using (8)
      end for
    end for
  end for
end for

---

the resistivity of the second layer material is smaller than that of the first layer, or $-1 < k < 0$ for the opposite case. As for the depth of the second layer, we presume it to be within the hemispherical region defined by the maximum distance of electrodes $|AM|$: $0 < h \le d_1$. Thirdly, for each candidate which represents a different setting of ρ_1, k and h, we calculate the corresponding function of apparent resistivity $\tilde{\rho}_a(d)$ given $d = d_0$ to d_1. Fourthly, the fitting errors between $\tilde{\rho}_a(d)$ and the actual value $\rho_a(d)$ can be calculated by summing the differences along d.

$$\text{Err} = \frac{\sum |\rho_a(d) - \tilde{\rho}_a(d)|}{N_d} \quad (10)$$

where N_d is the number of measurements along d. Subsequently, the Nearest Neighbour method is used with the norm between $\rho_a(d)$ and $\tilde{\rho}_a(d)$ as the calculation distance. We can approximate the parameters as the ones with the minimal fitting error.

D. Sensitivity Analysis

The sensitivity of electrodes-tissue interaction using the proposed tri-polar sensing system was tested using Finite Element Simulation (FES). The electric currents module of the COMSOL Multiphysics software (COMSOL Inc., Sweden) was used. The bi-polar sensing configuration was included for comparison.

As shown in Fig. 4(a) and (b), realistic scenarios were modelled with two and three electrodes inserted 10 mm into the tissue, simulating the bi-polar and tri-polar system respectively. This is to represent the forceps pushing the tissues and the deformation of tissue make it reshape around the electrode. The MUT is modelled as a $50 \times 50 \times 100$ mm block, and the electrodes were drawn in a similar shape as the forceps' jaw.

To simplify the simulation, the MUT was set to be pure conductive material with an unit resistivity (1 Ωm), and a direct current $I = 1$ mA was used. For the bi-polar configuration, the current was applied between the electrodes M and N, and the reciprocal voltage was measured from the same electrodes. For the tri-polar configuration, current I was applied on the electrode A, and the differential voltage was measured between M and
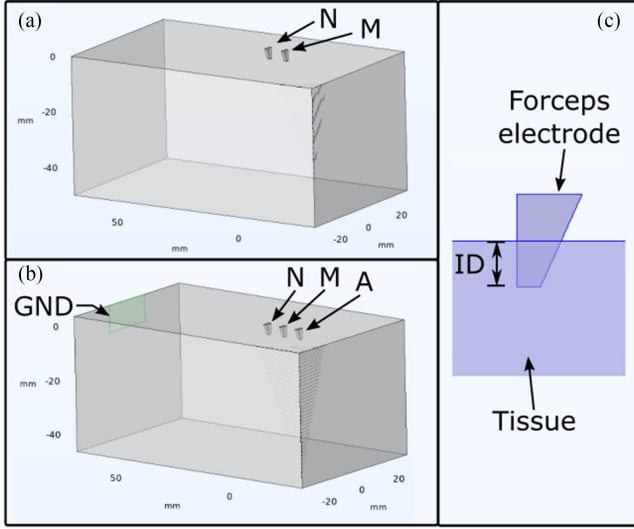
Fig. 4. The setup of FES for sensitivity analysis.

Fig. 5. The ranges of $|Z_m|$ in a bipolar configuration is presented as an errorbar plot (Top), and the ranges of $|Z_m|$ in a tripolar configuration are plotted in the (Middle). The simulated resistivity ρ_a is measured and calculated using different Δd (Bottom).

N. A relatively big area (10×20 mm) on the left side of the block was set as the electric ground (please refer to Fig. 4(b)). The contact impedance on the electrode due to the Helmholtz & Gouy-Chapman layer was not considered in the simulation. This was because of the difficult estimation of the contact impedance which varies from many factors such as material, current level, and excitation frequency. The presence of contact impedance was believed to bring in noise to a bi-polar configuration but cause little impact for a tri-polar configuration as interpreted in Section II-A.

For the bi-polar configuration, different distances between M and N were set from 2 to 10 mm with a step size of 2 mm. As for the tri-polar configuration, the distance of $|MN|$ was fixed at 2 mm, and five different values of $|AM|$ (2 to 10 mm) were examined. In addition, three immersed depths (ID = 0, 1 mm, and 2 mm) were applied on CSE and VME respectively. This lead to nine setting combinations.

According to the sensing principle of bi-polar [25] and tri-polar configurations (4), the measurement sensitivity is defined as $|Z_m| = \frac{V_{MN}}{I}$. Fig. 5 (Top) & (Middle) summarize the results of $|Z_m|$ in the first experiment. The results of the bi-polar configuration are plotted on the top and the results of the tri-polar configuration are plotted on the bottom. The distance d represents $|MN|$ for the bi-polar configuration and $|AM|$ for the tri-polar configuration.

Fig. 5 shows the range of $|Z_m|$ of the bipolar configuration (Top), and the tri-polar configuration (middle). The maximum values of $|Z_m|$ for both configurations always correspond to the measurement with ID = 0 for both CSE and VME. The minimum values are found to be the cases with ID = 2 mm for both CSE and VME. Fig. 5 also indicates that the sensitivity of $|Z_m|$ to the pressing depth ID is much lower in the tri-polar setup than that in the bi-polar setup. From the moment the forceps starts contacting the tissue to 2 mm pressing depth, $|Z_m|$ decreases from 12.7% ($d = 2$ mm) to 2.7% ($d = 10$ mm) for the tri-polar configuration, and 57.3% ($d = 2$ mm) to 46.2% ($d = 10$ mm) for
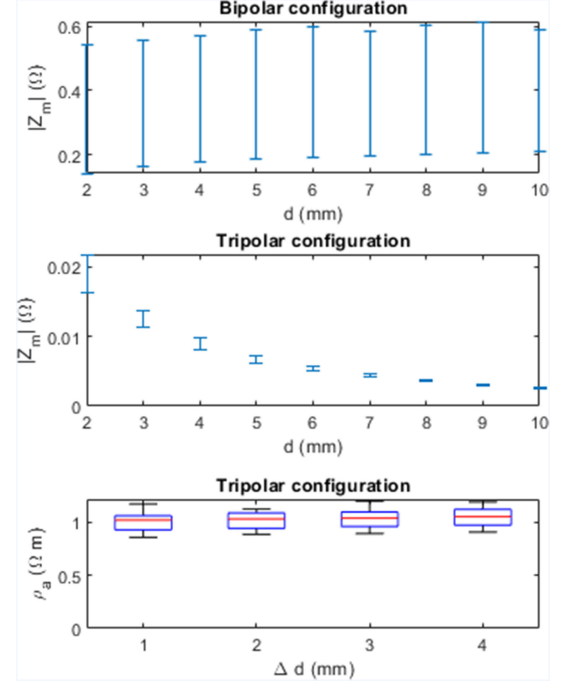
the bi-polar configuration. This improved feature is important to ensure the reliability of the RAEIS concept. Nevertheless, it is worth noting that the tri-polar configuration is sensitive to the electrodes' distance d, which should be controlled accurately in the real robotic system.

The impact of the tri-polar measurement accuracy due to a different setting of Δd was studied through simulation. In the simulation, the distance of $|MN|$ (i.e. Δd) was varied from 1 mm to 4 mm with a step size of 1 mm. Given $|AM|$ from 2 to 10 mm, the corresponding values of ρ_a were computed according to (4) and plotted in Fig. 5 (Bottom). No significant differences of the ρ_a values due to the different settings of Δd were found. Based on this finding, Δd was chosen to be 2 mm in the following study.

E. Sensing Circuit

To realize the above tri-polar EBI sensing, a circuit board was designed based on the front-end interface with potentiostatic excitation for AD5933 impedance sensor as presented in [35]. AD5933 is a single chip solution for high precision electrical impedance measurement. It has an on-board frequency generator for exciting an external complex impedance with a known frequency signal, and an on-board analog-to-digital converter (ADC) for measuring the response signal. The AD5933 can provide an excitation frequency up to 100 kHz, making it suitable for many types of bio-impedance measurement. However, this chip is originally designed for bi-polar impedance measurement. Therefore, a front-end interface to adapt the AD5933 to a tri-polar EBI sensing configuration is required.
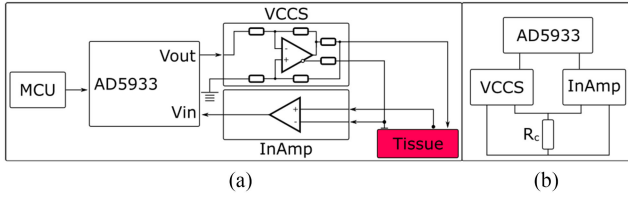
Fig. 6. (a) Simplified schematic of the sensing circuit. (b) Calibration setup.

As shown in Fig. 6, the front-end interface includes a Voltage Controlled Current Source (VCCS), controlled by the output of the AD5933, and an Instrumentation Amplifier (InAmp) feeding the voltage dropping at the voltage monitor electrodes into the AD5933 input. The integrated VCCS is a Howland-circuit using an operational amplifier with symmetric output, and it is used to provide galvanic excitation with a synchronized frequency as the output of AD5933. Considering that AD5933 has 4 output peak-to-peak voltage options (2 V, 1 V, 0.4 V and 0.2 V), the VCCS is designed to attenuate the output of AD5933 to offer 4 different current levels (1 mA, 0.5 mA, 0.2 mA and 0.1 mA). The possible maximum injected current is limited to be 1 mA as is required by the international standard for medical electrical instruments (IEC60601-7). The current circuit system aims to measure a load from 100 to 3000 Ω which is suitable for the targeted biological tissue sensing applications. To improve the sensing accuracy, the embedded code is able to control the AD5933 to execute a lower excitation current when the impedance is found exceeding the range. The voltage measured from the voltage monitor electrode is amplified by the InAmp with a gain of 1. A microcontroller board (Teensy 3.6) is used as the control unit to read the data from AD5933 and transfer the data to the connected laptop via USB.

F. System Calibration

1) Electric Circuit: After the circuit board was manufactured, a calibration procedure was conducted. As shown in Fig. 6(b), the calibration used 10 different known resistors (R_c) from 100 Ω to 3000 Ω. In addition, AD5933 was controlled to output different excitation frequencies from 10 kHz to 100 kHz with a step of 10 kHz. According to the calibration results, the average error rate is found to be 1%, and the maximum error is 2.3%.

2) Kinematics: The proposed RAEIS system coordinates a dual-arm collaboration and one ground electrode attached to the end of the MUT. One of the robotic arm carries the current source electrode (CSE) forceps and the other one carries voltage monitor electrode (VME) forceps.

As illustrated in Section II-C, it is critical to obtain the relative distance between two electrodes d accurately since the apparent resistivity $\rho_a(d)$ is sensitive to this parameter. Thus, calibration of the coordinates of two robotic arms is important. We first fixed both robotic arms to a static platform. By manually driving each robotic arm to 9 known points on the platform, the kinematic transformation matrix from the robot base coordinate to the global coordinate could be retrieved using the least squares approximation. The fitting errors were found to be 0.12 mm

and 0.09 mm for the CSE and the VME respectively. Although the exploited tri-polar configuration has less sensitivity to the electrodes' pressing depth, the variation due to this factor should be minimized. To ensure the pressing depth can be small and consistent, the forceps are controlled to move downwards slowly to each measuring site and stop the movement once a significant change of EBI value is detected.

III. Experimental Evaluation

The performance of the proposed system for subsurface critical tissue detection was evaluated including FES and experiments on realistic phantoms. The following perspectives are investigated during the system evaluation: 1. The RAEIS system can perform the scanning on a user-defined position and calculate the corresponding $\rho_a(d)$ values; 2. The RAEIS system can detect the subsurface non-homogeneous object successfully; 3. The system can provide accurate parameter estimation of the electrical resistivity of both materials and the depth of the interface.

As shown in Fig. 8(a), the experimental setup exploits two mono-polar robotic forceps (Intuitive Surgical Inc., U.S.) as electrodes. Specifically, one is used as the CSE and the other is used as the VME. Each forceps is fixed to the end of a UR3 robotic arm (Universal Robots A/S, Denmark). A laptop is used for controlling the robots and performing the measurements through the designed sensor board. In the current setup, we use 100 kHz as excitation frequency for the EBI sensing because it can provide fast sensing rate and a generally good performance for tissue classification [20].

A. Realistic Liver Cancer Experiment Based on FES

The concept of tri-polar sensing was first evaluated through a FES. Specifically, a scenario of finding subsurface hepatic cancerous tissue was constructed. The electric currents module of the COMSOL Multiphysics software was used here. As shown in Fig. 7, the normal liver tissue was drawn as a gray block (120 $\times$ 160 $\times$ 400 mm), and the abnormal tissue was represented by a pink block. Three different sizes of the abnormal tissue, namely 20 $\times$ 20 mm, 40 $\times$ 40 mm, and 60 $\times$ 60 mm, were tested. We used T_{20}, T_{40} and T_{60} to denote the above cases respectively. In addition, two electrodes with similar shapes as the real forceps' jaw were placed on the surface of the normal tissue. Three different settings were considered in the experiment:

- *Normal:* only normal tissue
- *T(4):* normal tissue with a subsurface tumor in the depth of 4 mm
- *T(8):* normal tissue with a subsurface tumor in the depth of 8 mm

Different simulation conditions were carried out including the center of two electrodes coincident to the center of the abnormal tissue in the X-Y direction and an offset between the centers. We used X_{Offset} and Y_{Offset} to denote the offset in the X and Y direction respectively. In the X direction, four offset values (± 4 mm and ± 8 mm) were tested. Only two values (4 mm and 8 mm) were tested for Y_{Offset} due to symmetry.
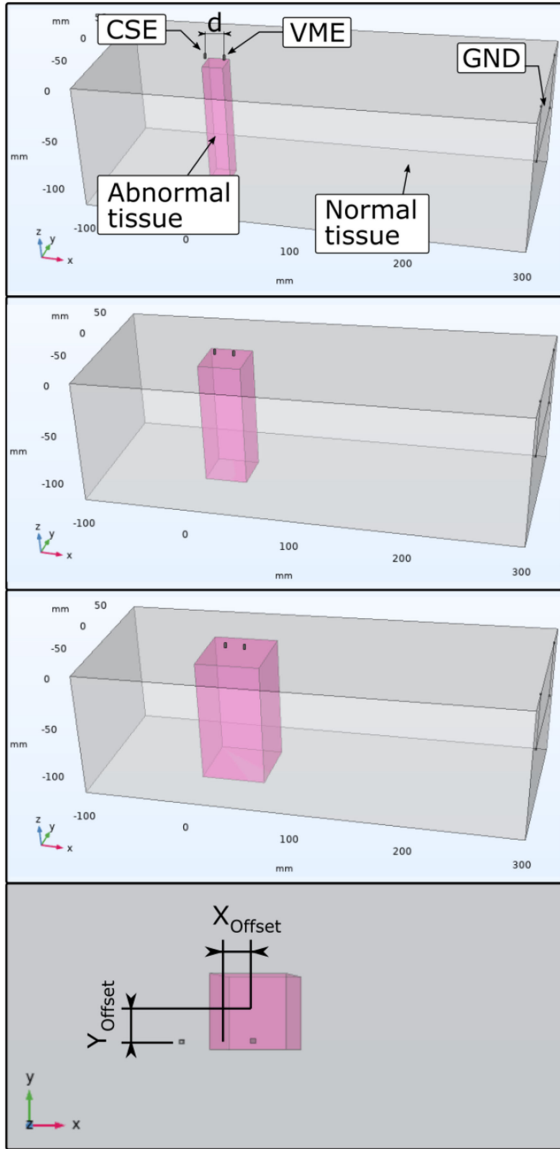
Fig. 7. The experimental setup of the FES for evaluating the system's performance in detecting subsurface abnormal tissue.

Fig. 8. The setup of the *ex vivo* animal tissue experiment.

The resistivity of normal and abnormal tissue was set to be 10 and 2.28 Ωm according to [36]. To simplify the simulation, a direct current $I = 1$ mA was applied on the CSE, and a big area (60×40 mm) on the right side of the tissue was grounded. Taking the current electrode as the origin, the electrical potential was measured on the tissue surface with varying d from 3 to 18 mm. Then the measured potential values were used to compute the values of ρ_a and Γ, based on which the existence of a tumor can be proven. The estimated values of ρ_1, ρ_2 and h were also calculated for conditions with subsurface abnormal tissue.

B. System Characterization With Saline Solutions

Before conducting experiments on ex vivo tissues, a saline solution experiment was carried out to evaluate whether the RAEIS system can measure material's resistivity accurately.
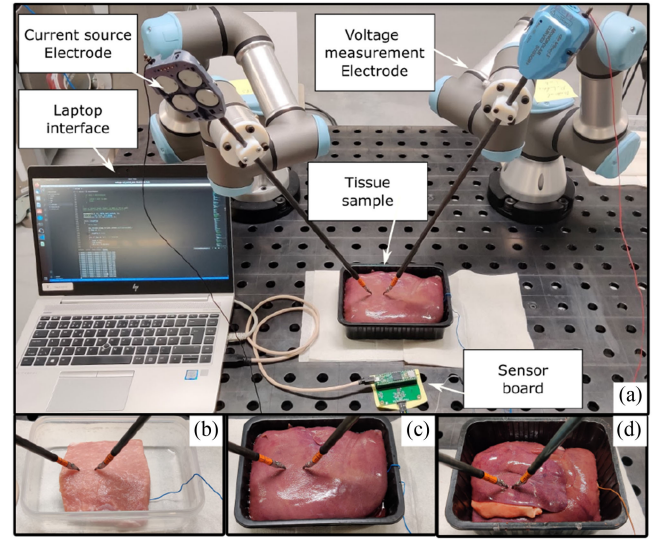
Standard saline solutions of three different concentrations including 0.1%, 0.2%, and 0.3% were made and put in a container. The impact of measurement accuracy due to the electrodes' immersed depth ID was also investigated in this study. Two ID settings corresponding to the maximum and minimum values as indicated in Section II-D were conducted. Specifically, the ID of both CSE and VME were set to 0 mm in the first condition and to 2 mm for the second condition. Then the RAEIS system performed the measurements on each saline solution and in each ID settings 10 times. During data collection, the CSE was first controlled to just touch the solution surface. Taking CSE as the origin, the VME was controlled to measure the electrical potential from 3 mm to 18 mm along a line with a step size of 1 mm. After the VME finishes moving each step, 10 continuous electrical potentials were measured and their mean value was used for the post-processing. In Section IV-B, the results of ρ_a were calculated and compared to the reference standard values.

C. Ex Vivo Animal Tissue Experiment

An experiment based on ex vivo porcine tissues was designed and carried out for the evaluation of the developed system. This experiment simulated a realistic scenario where the surgeon is required to search for an early stage hepatic cancer which grows under a thin layer of healthy tissue. To investigate a place-of-interest, the surgeon controls the tip of the CSE to touch the target tissue surface, and then the VME completes the electric potential scanning automatically. Based on the measurements, the system can inform the surgeon whether there is an abnormal tissue in the subsurface region.

As shown in Fig. 8, the tissue samples were placed in a plastic container where a copper plate was attached to the right bottom of the tissue samples as the ground electrode. A comparative experiment was designed and conducted on three phantoms including:
- **Phantom-M**: only muscle tissue (Fig. 8(b))
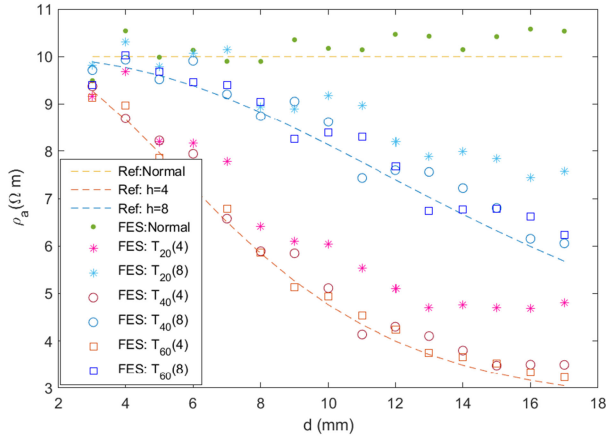- **Phantom-L**: only liver tissue (Fig. 8(c))

Fig. 9. The apparent resistivity from simulation (FES) and analytical calculation (Ref) in three simulation conditions: *Normal*, *T(4)* and *T(8)*.

- **Phantom-LM**: phantom combining liver and muscle tissues (Fig. 8(d))

Phantom-LM was made out of putting the muscle ($60 \times 60 \times 20$ mm) under a thin layer of liver tissue whose thickness was between 5 mm and 10 mm. In this experiment, the muscle was used to simulate cancerous tissue, since they have similar electrical resistivities at 100 kHz excitation frequency according to [37].

During the measurement, the CSE was first placed on the tissue surface, and the VME was controlled to measure the electrical potential from 3 mm to 18 mm from left to right with a step size of 1 mm. 10 continuous readings of electrical potentials were recorded after the VME finished the movement in each step. For each phantom, the measurements were repeated ten times. Although a fixed pressing depth of 2 mm were set for both CSE and VME, the immersed depth can be different and generally <2 mm considering tissue deformation and different tissue stiffness. We applied a low pass filter to the measured data and calculated the apparent resistivities. Results and analysis are provided in Section IV-C.

IV. RESULTS

A. Experimental Results of FES

The apparent resistivity ρ_a with $d = 3$ mm to 17 mm is computed based on the simulation results. We first present the results without center offset in Fig. 9. The values of ρ_a for *Normal* are plotted in green dots. Results of *T(h=4)* and *T(h=8)* are presented in red-related and blue-related colors. In addition, we use star, circle and square for results obtained from different size settings of the abnormal tissue (20×20 mm, 40×40 mm, and 60×60 mm) respectively. The analytical results of three conditions are computed using (8) and plotted as dash lines for comparison. The root mean square errors (RMSE) between the FES results and the analytical results are calculated, and found to be relatively small (≤ 0.37 Ωm) for Condition *Normal* and conditions T_{40}, and T_{60}. For the cases of T_{20}, the RMSE is slightly higher, which are 1.12 Ωm and 1.02 Ωm for condition $T_{20}(4)$ and $T_{20}(8)$ respectively. Some small variations of
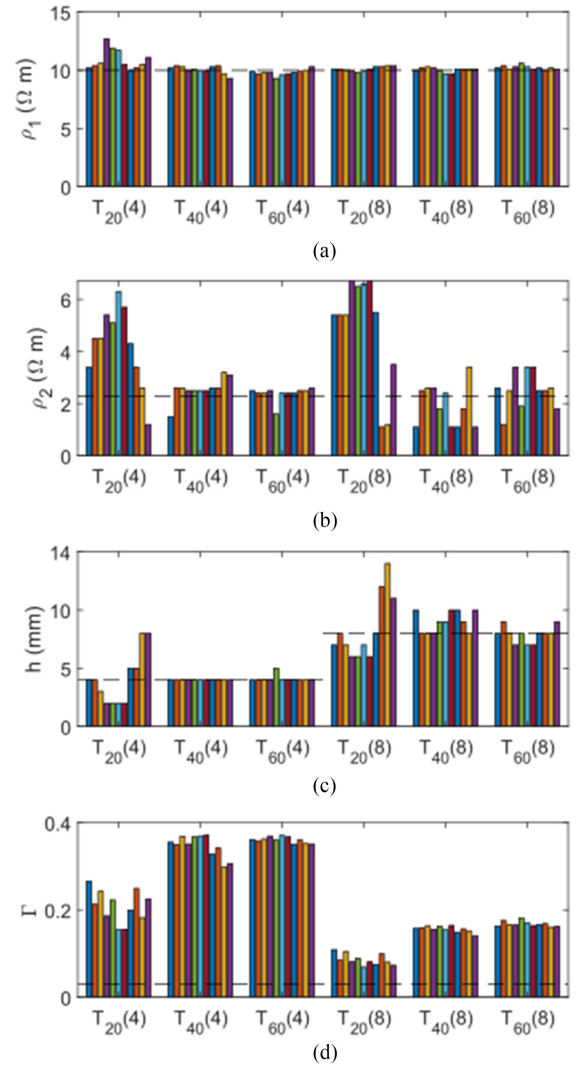

Fig. 10. Simulation results including the estimated values of ρ_1, ρ_2, h and Γ. The results are organized into 6 subgroups representing different subsurface object size and depth. For each subgroup, 11 results calculated from simulations with different offset settings are shown: From left to right, $(X_{\text{Offset}}, Y_{\text{Offset}}) = (0, 0)$, $(0, 8)$, $(0, 4)$, $(-4, 8)$, $(-4, 4)$, $(-8, 8)$, $(-8, 4)$, $(4, 8)$, $(4, 4)$, $(8, 8)$, $(8, 4)$.

FES results are observed. The reason is suspected due to the regenerated meshing of the model in each iteration during FES. This influence is hard to avoid even though an "Extremely fine" meshing setting is implemented.

Fig. 10 summarizes the results of the FES experiment in different settings. The bar plots in Fig. 10(a), (b) and (c) show the estimated values of ρ_1, ρ_2 and h based on the proposed method respectively, and the corresponding reference values are shown as dash lines. Fig. 10(d) shows the calculated Γ values which can be used for subsurface structure detection. The dash line in Fig. 10(d) represents the Γ value in the *Normal* condition. The results are organized in six subgroups with different subsurface object size and different depth. In each subgroup, eleven results are shown, presenting the offset setting $(X_{\text{Offset}}, Y_{\text{Offset}})$ (unit: mm) in the following combinations: $(0, 0)$, $(0, 8)$, $(0, 4)$, $(-4, 8)$, $(-4, 4)$, $(-8, 8)$, $(-8, 4)$, $(4, 8)$, $(4, 4)$, $(8, 8)$, $(8, 4)$. The

TABLE I
SIMULATION RESULTS INCLUDING THE ESTIMATED VALUES
(MEAN ± STD. DEV.) OF THE RESISTIVITY OF THE SUPERFICIAL TISSUE ρ_1,
THE RESISTIVITY OF THE SUBSURFACE TISSUE ρ_2, THE DEPTH OF THE
SUBSURFACE TISSUE h AND THE DETECTION CRITERIA Γ

	ρ_1 [Ωm]	ρ_2 [Ωm]	h [mm]	Γ
$T_{20}(4)$	10.8 ± 0.9	4.2 ± 1.5	4.1 ± 2.3	0.21 ± 0.04
$T_{40}(4)$	10.1 ± 0.3	2.6 ± 0.4	4 ± 0	0.35 ± 0.03
$T_{60}(4)$	9.8 ± 0.2	2.4 ± 0.3	4.1 ± 0.3	0.360 ± 0.007
$T_{20}(8)$	10.1 ± 0.2	4.9 ± 2.1	8.4 ± 2.7	0.086 ± 0.010
$T_{40}(8)$	10.0 ± 0.2	2.0 ± 0.8	9.0 ± 0.9	0.160 ± 0.006
$T_{60}(8)$	10.2 ± 0.2	2.5 ± 0.7	7.9 ± 0.7	0.170 ± 0.007

mean and standard deviation of ρ_1, ρ_2, h and Γ in six subgroups are summarized in Table I.

We perform the parameter estimation of ρ_1, ρ_2 and h using the search algorithm as detailed in Section II-C. For all the conditions with abnormal tissue, decreasing trends of $\rho_a(d)$ against d are observed, indicating the hidden object has a lower resistivity. Therefore, the range of k for sampling is set from -0.1 to -0.9 with a step of 0.1. In addition, the candidate pool is created with h from 1 mm to 18 mm with a step size of 1 mm, and 20 equal step samples of α from 0 to $2k/(1-k)$. Subsequently, the fitting errors between each candidate and the simulation results are calculated. The researching algorithm take an average of 0.03 s to find the best match. The estimated parameters of different experimental conditions are reported in Table. I. The results show that the estimated values of ρ_1 is generally accuracy ranging from 9.9 Ωm to 10.2 Ωm, given the actual setting of 10 Ωm. With respect to the resistivity of the subsurface material, the estimation accuracy is found to be low, especially when the abnormal tissue size is small and it is located deeply. The error rate is found to be relatively low for a bigger size of abnormal tissue (9.6% and 14% for the cases of T_{60}), and becomes big when the abnormal tissue was small such as 137% for Condition $T_{20}(h=8)$. In addition, the estimated depth of the interface is relatively accurate. Specifically, the depth of conditions with h = 4 mm could be all detected correctly. However, the accuracy is slightly low for the conditions with h = 8 mm as two cases are reported to be 10 mm and 7 mm.

B. Characterization Results Using Saline Solutions

The characterization results using three saline solutions (0.1%, 0.2%, and 0.3%) and two ID settings are presented in Fig. 11. Also, the corresponding electric resistivities of the three saline solutions (5.9, 3.0, and 2.0 Ωm), according to IEC60746-3, are plotted as references.

We calculate the mean and standard deviation of all the data using the same ID and for a specific saline solution. The values of ρ_a are found to be 6.0 ± 0.46 Ωm and 6.2 ± 0.49 Ωm for 0.1% saline solution using a 0 mm and 2 mm ID respectively. For 0.2% saline solution, the computed ρ_a are 3.5 ± 0.26 Ωm and 3.2 ± 0.3 Ωm for ID = 0 mm and 2 mm. The results of 0.3% saline solution using 0 mm and 2 mm ID are 2.2 ± 0.13 Ωm and 2.2 ± 0.19 Ωm. The results indicate a small impact of the measurement accuracy due to the electrode immersed depth, and a good accuracy.

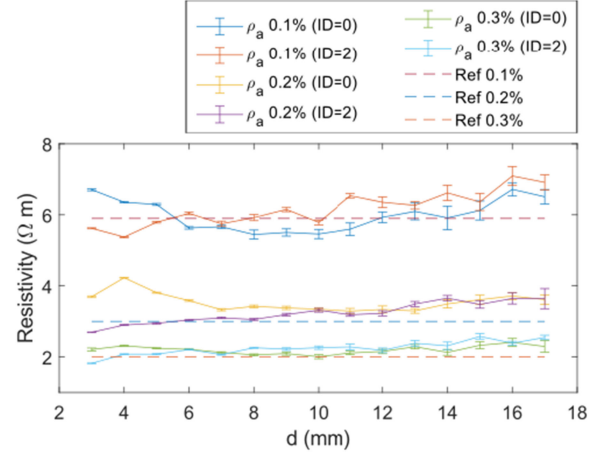
Fig. 11. The measured apparent resistivity $\rho_a(d)$ of 0.1%, 0.2% and 0.3% concentration saline solutions by the RAEIS system and the corresponding reference values according to IEC60746-3.
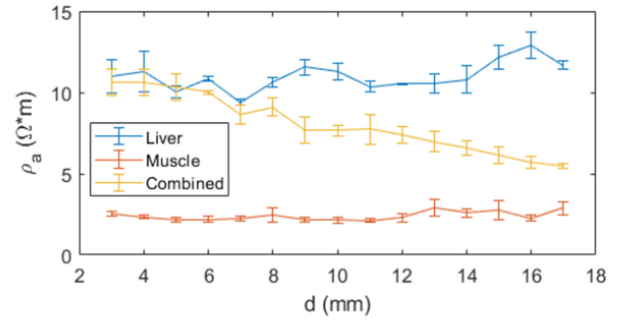

Fig. 12. The ρ_a values as a function of d obtained from 3 phantoms.

C. Ex Vivo Animal Tissue Experiment

The mean values and standard deviations of $\rho_a(d)$ measured on three phantoms are plotted in Fig. 12. According to the experimental results, the ρ_a values of **Phantom-M** and **Phantom-L** are generally flat, and their overall mean values are found to be 11.0 Ωm and 2.4 Ωm respectively. A decreasing trend of ρ_a from 10.6 Ωm to 5.5 Ωm is observed for **Phantom-LM**. This finding is also coherent with the Γ values, which are found to be 0.11, 0.08 and 0.22 for **Phantom-M**, **Phantom-L**, and **Phantom-LM** respectively. The experimental results indicate that the differences among three phantoms are significant, and a simple threshold on the Γ values can be implemented for detecting the existence of the hidden muscle.

Furthermore, the parameter estimation of ρ_1, ρ_2 and h are conducted on the mean values of $\rho_a(d)$ in condition **Phantom-LM**. Again, the search algorithm is used and the parameters are estimated to be $\rho_1 = 10.99$ Ωm, $\rho_2 = 3.66$ Ωm, $h = 6$ mm. The fitting error is reported to be Err=0.016 Ωm.

V. DISCUSSION

According to the results of the simulations (Fig. 5) and experiments (Fig. 11), the tri-polar configuration is demonstrated to have a low sensitivity to the forceps' immersed depth. This

parameter is generally difficult to measure due to the tissue deformation. Thus, decreasing the sensitivity to the forceps' immersed depth can significantly improve the sensing stability. Nevertheless, bigger variations are observed when d is small. This may suggest starting the measurement with a bigger d in the future setup. In practice, both CSE and VME can be controlled to contact the tissue surface and press slightly. Thus, a reliable measurement can be guaranteed and no tissue damage would happen. Although the proposed tri-polar system has a higher sensitivity to d, which is the distance between the tips of CSE and VME, this parameter is relatively easier to control through the robot's kinematics or using vision tracking facilities such as [38].

The capability of using the RAEIS system for detecting subsurface non-homogeneous tissue are demonstrated by experiments based on FES and ex vivo tissues. According to the experimental results, the apparent resistivity ρ_a shows an increasing/decreasing trend with the increase of d if a subsurface non-homogeneous object exists. This is the result from the reflected current as interpreted in (6). Based on this theory, a parameter Γ, which is the relative standard deviation of ρ_a, can be used for determining whether the subsurface object exists. When the MUT is homogeneous, a nearly constant ρ_a can be observed, and thus Γ is close to 0. In contrast, the non-homogeneity of the MUT can be detected if Γ is found to be relatively big. Although the use of relative standard deviation for the subsurface tissue detection task is demonstrated, Γ is found to accumulate errors due to noise. The detection criteria will seek to be improved in the future.

The depth of the interface h and the electrical resistivity of both materials can be approximated given sufficient data sets of $\rho_a(d)$. As demonstrated in the FES experiments (Fig. 10), the estimated parameters of ρ_1 and h are relatively accurate. The accuracy of the estimated ρ_2 may depend on the size of the subsurface object and whether the sensing electrodes are above the subsurface object. A relatively high accuracy of the estimated ρ_2 is found when the subsurface object has a relatively bigger size. But if the subsurface abnormal tissue is small and away from the sensing electrodes, only part of the reflected current (7) is counted in the measured impedance. This noise would decrease the estimation accuracy of ρ_2 and h. In this case, the ρ_a values can be fitted to a lower ρ_2 and a bigger h, or a bigger ρ_2 and a smaller h. Nevertheless, all the experimental conditions with abnormal tissue could be detected successfully according to the Γ values. As indicated in Table I, the Γ values of all the conditions are bigger than the Γ value for Condition *Normal* (0.03). To determine the existence of an abnormal hidden layer simply a threshold between 0.03 and 0.068 can be used. This implies a reliable capability for using the proposed RAEIS system in subsurface abnormal tissue detection. In the ex vivo study, the size of the muscle is similar to the FES setup T_{60}. The results of the ex vivo experiments confirm the findings in FES, demonstrating that the proposed system is able to detect the presence of the subsurface tissue and approximate its depth and resisitivity. Based on the experimental results, we can reasonably expect a lower accuracy of parameter estimation when the subsurface material has a relatively smaller size. To

address this issue, we are working towards a machine learning based algorithm to estimate the related parameters based on multiple scanning in a local region. In addition, the estimated depth h is found to be 6 mm in the experiment with ex vivo tissues. Since the thickness of soft tissue is difficult to measure accurately, this parameter is evaluated qualitatively and we find the estimated value is in a reasonable range. Moreover, the estimated resistivity of liver is 10.99 Ωm which is very close to the mean value measured on **Phantom-L** 11.0 Ωm (99.9% accuracy). The estimated resistivity of muscle is found to be 3.66 Ωm which is bigger than the mean value of **Phantom-M** 2.4 Ωm (47.5% accuracy). This is possibly because the interface between liver and muscle is not flat. In this case, EIT technology based on more sophisticated algorithms and more measurement sites may improve the estimation accuracy. The integration and test will be one of the main focuses in our future study.

Theoretically, the proposed system can detect very deep regions by increasing the distance between two forceps d. However, as indicated in (3), the measured voltage difference decreases with the increase of d, and the signal can be immersed by noise when d is set too big. In addition, the start scanning position of VME cannot be too close to CSE. This is on one hand to prevent the collision between the two forceps effectively; on the other hand to decrease the impact from the forceps' pressing depth (Fig. 5). Future work will investigate using varying Δd in the scanning process to achieve a balance between measurement accuracy and scanning efficiency.

In addition, the real surgical scenario may have complicated anatomical structure and tissue moving. The related factors can reduce the sensing accuracy. To minimize this impact, 3D reconstruction and tracking based on endoscopic cameras can be involved for guiding the scanning. This will be another focus in the future study. Also, the future study will investigate the performance of the RAEIS system when it works on a tissue surface with blood or fluid. Another focus of the future study will investigate the sensitivity of the RAEIS system in the detection of small subsurface tissue.

VI. Conclusion

In this study, we present a novel tri-polar RAEIS system aiming to assist the surgeon in finding subsurface non-homogeneous tissue structure. The proposed system was realized by incorporating two forceps, one for providing excitation current source and the other one for measuring voltage in a series of locations. Without involving new hardware to the field, the proposed method can be achieved by using already established hardware for most medical robots. This can greatly speed up its applications in the operation room.

The proposed RAEIS system has been characterized and demonstrated to have sufficient sensing stability with minimal influence due to the forceps' pressing depth. By exploiting the robotic technology the EBI scanning is done autonomously and efficiently. A series of experiments were conducted to evaluate the proposed system in terms of detecting a hidden layer of abnormal tissue. According to the experimental results both in FES and on ex vivo tissues, the developed system was demonstrated

to detect a different material in a deeper region successfully. Also, the material resistivity and the depth of the subsurface tissue can be estimated effectively using the proposed search algorithm. This promising result convince us to further improve this system and prepare it for more realistic experimental study in the next step.

ACKNOWLEDGMENT

REFERENCES

[1] Intuitive Surgical, Inc., "Q2 2020 Intuitive Investor Presentation," 2020. [Online]. Available: https://isrg.gcs-web.com/static-files/7b0470fb-cfd2-456a-b6eb-24af76d68f6d

[2] R. H. Taylor *et al.*, "Medical robotics and computer-integrated surgery," in *Springer Handbook Robot.*, 2016, pp. 1657–1684.

[3] G. P. Moustris *et al.*, "Evolution of autonomous and semi-autonomous robotic surgical systems: A review of the literature," *Int. J. Med. Robot. Comput. Assist. Surg.*, vol. 7, no. 4, pp. 375–392, 2011.

[4] M. Goetz *et al.*, "In vivo confocal laser laparoscopy allows real time subsurface microscopy in animal models of liver disease," *J. Hepatol.*, vol. 48, no. 1, pp. 91–97, 2008.

[5] R. Sullivan *et al.*, "Global cancer surgery: Delivering safe, affordable, and timely cancer surgery," *Lancet Oncol.*, vol. 16, no. 11, pp. 1193–1224, 2015.

[6] I. Opitz *et al.*, "Bleeding remains a major complication during laparoscopic surgery: Analysis of the salts database," *Langenbeck's Arch. Surg.*, vol. 390, no. 2, pp. 128–133, 2005.

[7] P. L. Kubben *et al.*, "Intraoperative MRI-guided resection of glioblastoma multiforme: A systematic review," *Lancet Oncol.*, vol. 12, no. 11, pp. 1062–1070, 2011.

[8] M. S. Block and C. Chandler, "Computed tomography-guided surgery: Complications associated with scanning, processing, surgery, and prosthetics," *J. Oral Maxillofac. Surg.*, vol. 67, no. 11, pp. 13–22, 2009.

[9] V. Penza *et al.*, "Enhanced vision to improve safety in robotic surgery," in *Handbook Robotic Image-Guided Surg.* Elsevier, 2020, pp. 223–237.

[10] V. Penza *et al.*, "The GPS for surgery: A user-centered evaluation of a navigation system for laparoscopic surgery," *Int. J. Med. Robot. Comput. Assist. Surg.*, vol. 16, no. 5, pp. 1–13, 2020.

[11] S. Sound *et al.*, "Intraoperative tumor localization and tissue distinction during robotic adrenalectomy using indocyanine green fluorescence imaging: A feasibility study," *Surg. Endoscopy*, vol. 30, no. 2, pp. 657–662, 2016.

[12] W. K. Huh *et al.*, "Optical detection of high-grade cervical intraepithelial neoplasia in vivo: Results of a 604-patient study," *Amer. J. Obstet. Gynecol.*, vol. 190, no. 5, pp. 1249–1257, 2004.

[13] A. L. Vahrmeijer *et al.*, "Image-guided cancer surgery using near-infrared fluorescence," *Nat. Rev. Clin. Oncol.*, vol. 10, no. 9, pp. 507–518, 2013.

[14] Y. Chen *et al.*, "Review of surgical robotic systems for keyhole and endoscopic procedures: State of the art and perspectives," *Front. Med.*, vol. 14, pp. 382–403, 2020.

[15] G. Ceccarelli *et al.*, "Evolving technologies in the operating room for minimally invasive pancreatic surgery," in *Minimally Invasive Surgery of the Pancreas*. Milano, Italy: Springer, 2018, pp. 15–26.

[16] A. Stilli *et al.*, "Pneumatically attachable flexible rails for track-guided ultrasound scanning in robotic-assisted partial nephrectomy-a preliminary design study," *IEEE Robot. Automat. Lett.*, vol. 4, no. 2, pp. 1208–1215, Apr. 2019.

[17] A. Faragasso *et al.*, "Novel uniaxial force sensor based on visual information for minimally invasive surgery," in *Proc. IEEE Int. Conf. Robot. Automat.*, 2014, pp. 1405–1410.

[18] T. Li, C. Shi, and H. Ren, "A high-sensitivity tactile sensor array based on fiber bragg grating sensing for tissue palpation in minimally invasive surgery," *IEEE/ASME Trans. Mechatronics*, vol. 23, no. 5, pp. 2306–2315, Oct. 2018.

[19] O. G. Martinsen and S. Grimnes, *Bioimpedance and Bioelectricity Basics*. New York, NY, USA: Academic Press, 2011.

[20] Z. Cheng *et al.*, "A new venous entry detection method based on electrical bio-impedance sensing," *Ann. Biomed. Eng.*, vol. 46, no. 10, pp. 1558–1567, 2018.

[21] Z. Cheng *et al.*, "Smartprobe: A bioimpedance sensing system for head and neck cancer tissue detection," *Physiol. Meas.*, vol. 41, no. 5, 2020, Art. no. 054003.

[22] Y. Dai, Y. Xue, and J. Zhang, "Drilling electrode for real-time measurement of electrical impedance in bone tissues," *Ann. Biomed. Eng.*, vol. 42, no. 3, pp. 579–588, 2014.

[23] B. G. Pedro *et al.*, "Analytical model for blood glucose detection using electrical impedance spectroscopy," *Sensors*, vol. 20, no. 23, 2020, Art. no. 6928.

[24] E. K. Murphy *et al.*, "Comparative study of separation between ex vivo prostatic malignant and benign tissue using electrical impedance spectroscopy and electrical impedance tomography," *Physiol. Meas.*, vol. 38, no. 6, pp. 1242–1261, 2017.

[25] Z. Cheng *et al.*, "Design and integration of electrical bio-impedance sensing in a bipolar forceps for soft tissue identification: A feasibility study," in *Proc. Int. Conf. Elect. Bioimpedance*, 2019, pp. 3–10.

[26] K. L. Schwaner *et al.*, "Robotically assisted electrical bio-impedance measurements for soft tissue characterization: A feasibility study," in *Proc. Hamlyn Symp. Med. Robot. Hamlyn Centre*, 2019, pp. 31–32.

[27] Z. Cheng *et al.*, "Design and integration of electrical bio-impedance sensing in surgical robotic tools for tissue identification and display," *Front. Robot. AI*, vol. 6, pp. 1–8, 2019.

[28] S. Sherif *et al.*, "Integration of tri-polar microelectrodes for performance enhancement of an impedance biosensor," *Sens. Bio-Sens. Res.*, vol. 28, 2020, Art. no. 100329.

[29] K. S. Cole and R. H. Cole, "Dispersion and absorption in dielectrics i. alternating current characteristics," *J. Chem. Phys.*, vol. 9, no. 4, pp. 341–351, 1941.

[30] U. Pliquett *et al.*, "Testing miniaturized electrodes for impedance measurements within the β-dispersion-a practical approach," *J. Elect. Bioimpedance*, vol. 1, no. 1, pp. 41–55, 2019.

[31] M. Amini, J. Hisdal, and H. Kalvøy, "Applications of bioimpedance measurement techniques in tissue engineering," *J. Elect. Bioimpedance*, vol. 9, no. 1, pp. 142–158, 2018.

[32] Z. Cheng and T. R. Savarimuthu, "A novel robot assisted electrical impedance scanning system for subsurface object detection," *Meas. Sci. Technol.*, vol. 32, no. 8, 2021, Art. no. 085902.

[33] P. Kearey, M. Brooks, and I. Hill, *An Introduction to Geophysical Exploration*. Hoboken, NJ, USA: John Wiley & Sons, 2013.

[34] J. J. Jakosky, *Exploration Geophysics*. Trija Publishing Company, 1950.

[35] U. Pliquett and A. Barthel, "Interfacing the ad5933 for bio-impedance measurements with front ends providing galvanostatic or potentiostatic excitation," *J. Phys.: Conf. Ser.*, vol. 407, p. 012019, 2012.

[36] D. Haemmerich *et al.*, "Electrical conductivity measurement of excised human metastatic liver tumours before and after thermal ablation," *Physiol. Meas.*, vol. 30, no. 5, pp. 459–466, 2009.

[37] D. Andreuccetti, R. Fossi and C. Petrucci, "An internet resource for the calculation of the dielectric properties of body tissues in the frequency range 10 hz-100 Ghz," *IFAC-CNR*, Florence, Italy, 1997.

[38] D. Bouget *et al.*, "Vision-based and marker-less surgical tool detection and tracking: A review of the literature," *Med. Image Anal.*, vol. 35, pp. 633–654, 2017.